CHEMISTRY OF MATERIALS

pubs.acs.org/cm

Article

Robot-Accelerated Perovskite Investigation and Discovery

Zhi Li, Mansoor Ani Najeeb, Liana Alves, Alyssa Z. Sherman, Venkateswaran Shekar, Peter Cruz Parrilla, Ian M. Pendleton, Wesley Wang, Philip W. Nega, Matthias Zeller, Joshua Schrier,* Alexander J. Norquist,* and Emory M. Chan*

Cite This: *Chem. Mater.* 2020, 32, 5650–5663

Read Online

ACCESS | Metrics & More | Article Recommendations | Supporting Information

ABSTRACT: Metal halide perovskites are a promising class of materials for next-generation photovoltaic and optoelectronic devices. The discovery and full characterization of new perovskite-derived materials are limited by the difficulty of growing high quality crystals needed for single-crystal X-ray diffraction studies. We present an automated, high-throughput approach for metal halide perovskite single crystal discovery based on inverse temperature crystallization (ITC) as a means to rapidly identify and optimize synthesis conditions for the formation of high quality single crystals. Using this automated approach, a total of 8172 metal halide perovskite synthesis reactions were conducted using 45 organic ammonium cations. This robotic screening increased the number of metal halide perovskite materials accessible by an ITC synthesis route by more than 5-fold and resulted in the formation of two new phases, $[C_2H_7N_2][PbI_3]$ and $[C_7H_{16}N]_2[PbI_4]$. This comprehensive data set allows for a statistical quantification of the total experimental space and of the likelihood of large single crystal formation. Moreover, this data set enables the construction and evaluation of machine learning models for predicting crystal formation conditions. This work is a proof-of-concept that combining high throughput experimentation and machine learning accelerates and enhances the study of metal halide perovskite crystallization. This approach is designed to be generalizable to different synthetic routes for the acceleration of materials discovery.

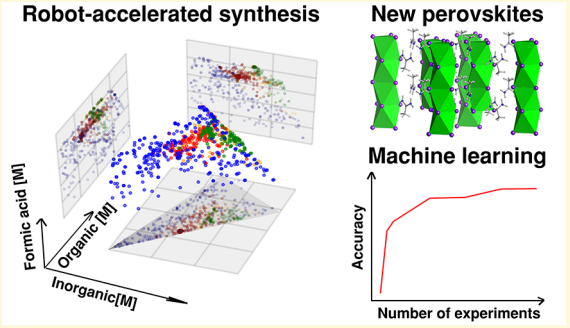

INTRODUCTION

Metal halide perovskites[1,2] can exhibit tunable electronic properties[3−6] that are leveraged in optoelectronic,[7−11] thermoelectric,[12,13] and photovoltaic devices,[14−19] for which power conversion efficiencies of 24.2% have been achieved.[20] The composition and structure of metal halide perovskites determine electronic properties such as carrier mobilities and band structure.[6,21] However, access to suitable crystalline perovskites for detailed characterization of their structure and physical properties has been hindered by limited understanding of the underlying processes through which large high quality single crystals grow.

A diverse array of synthetic routes exist for the growth of metal halide perovskite single crystals, including antisolvent vapor-assisted crystallization,[22−25] seeded crystal growth,[26,27] slow evaporation,[28,29] and inverse temperature crystallization (ITC).[30−33] ITC is a promising choice for structural studies of new perovskite materials because it can be used to grow high quality crystals without the need for long growth times. To date, metal halide perovskite ITC behavior, in which the solubility decreases with increased temperature, has been observed for only four compositions: methylammonium lead iodide ($MAPbI_3$), methylammonium lead bromide ($MAPbBr_3$), formamidinium lead iodide ($FAPbI_3$), and formamidinium lead bromide ($FAPbBr_3$).[34−36] Extension of the ITC route to new chemical systems is slow because successful crystal growth using this technique requires the simultaneous optimization of a large number of interdependent parameters such as reagent concentration and reaction temperature, necessitating many experimental trials.

High-throughput synthetic approaches are well-suited for efficiently exploring large experimental parameter spaces.[37] Such approaches have been used to search for new organic reactions,[38−41] optimize synthetic conditions of inorganic materials,[42−45] and discover new inorganic materials for energy, catalysis, and sensing applications.[46−52] Specifically, high-throughput synthetic approaches have been used to explore the formation of metal halide perovskites in the form of thin-films,[53,54] polycrystalline samples,[50] nanocrystals,[55,56] and, recently, as single crystals produced by antisolvent vapor-assisted crystallization.[52] The application of such high-throughput approaches to the growth of metal halide

Received: March 17, 2020
Revised: June 4, 2020
Published: June 4, 2020

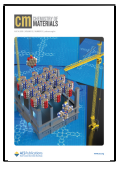

https://dx.doi.org/10.1021/acs.chemmater.0c01153
Chem. Mater. 2020, 32, 5650–5663

perovskite single crystals requires the adaptation of experimental routes to ensure compatibility with liquid handling robotics. Optimal utilization of high-throughput data sets requires the capture of nuanced experimental details that enable subsequent analysis with machine learning models, which have shown promise in this domain.[52−55,57−63]

In this report, we describe a series of high-throughput metal halide perovskite crystal growth experiments, using a new platform for Robot-Accelerated Perovskite Investigation and Discovery (RAPID). A total of 8172 individual crystallization reactions were performed via ITC across 45 chemical systems. This RAPID screening increased the number of metal halide perovskite systems for which ITC conditions can be used to grow crystals by more than 5-fold. Additionally, our work resulted in the discovery of two new compounds, $C_2H_7N_2PbI_3$ and $(C_7H_{16}N)_2PbI_4$. Experiment generation and data management in the high-throughput workflow were enabled by a software pipeline, ESCALATE (Experiment Specification, Capture and Laboratory Automation Technology),[64] to both capture a complete record of the high-throughput experiments and observational data, and to format those data for use in machine learning studies. The resulting data set was used to train machine learning models for each chemical system, demonstrating the utility of our high-throughput approaches to metal halide perovskite crystal growth.

RESULTS AND DISCUSSION

Robot Accelerated Perovskite Workflow. A high-throughput robotic synthesis of perovskites imposes three practical constraints. First, the use of a liquid handling robot necessitates that all reagents be dispensed as homogeneous solutions. The solubilities of the reactive species thus define the upper bounds of the chemical concentration space in which reactions can be performed, while the lower bounds are necessarily zero (i.e., solvent only). If data are to be used for subsequent modeling, then software such as ESCALATE[64] must capture all of these experimental details, even for manual operations such as the preparation of stock solutions. Second, chemical compatibility with the robot precludes the use of strong acids, such as HI. Only weak acids, such as formic acid, are allowed in the experiment to avoid robot damage. Third, heating block limitations, as well as the flash point of solvents, constrain reaction temperatures from 95 °C to room temperature. We classify any synthesis satisfying these constraints as "RAPID".

In this paper, we describe a RAPID ITC route for the formation of metal halide perovskite single crystals. The solubilities of all reactants are measured (see Table S2 in the Supporting Information, SI) to ensure that stock solutions utilize the highest possible concentrations of the dissolved species, maximizing the amount of chemical space available for exploration. The liquid handling robot pipettes four different types of stock solutions into 96 well microplates: (1) a stock solution of lead(II) halide and the selected organoammonium halide, included to increase the solubility of the lead halide; (2) a stock solution of the selected organoammonium halide; (3) pure solvent; and (4) neat formic acid. The stock solutions are prepared in one of three solvents: γ-butyrolactone (GBL), dimethyl sulfoxide (DMSO), and dimethylformamide (DMF) (see Table S2 for the solvent used in each chemical system). After dispensing the reagent solutions, the liquid handler vortexes and heats the microplates to ensure that the solutions are fully mixed. After vortexing is complete, the resulting perovskite solutions are heated undisturbed for 2.5 h to allow for crystal growth. An experimental flowchart describing reagent selection, benchtop testing, reaction components, stock solution preparation, and robotic reaction is shown in Figure S4. All variables with explanation of their bounds and values in the experiments are specified in Table S3, and detailed experimental procedures are available in the SI. Initial experiments focused on Pb^{2+} and I^-, the most explored metal and halide combination in metal halide perovskites. Iodides are generally more stable than chlorides and bromides and have narrower band gaps more appropriate for solar applications.[5,65] Using formic acid promotes crystallization by shifting the lead iodide equilibrium from colloidal cluster species to ionic species, reducing the crystallization onset temperature.[30,66] Formic acid is a sufficiently weak acid to be compatible with the NIMBUS liquid handling robot used in this work.

The selection of specific reactant concentrations, with corresponding solution volumes, is performed using a quasi-random sample of the possible experimental composition parameters through ESCALATE.[64] Additionally, ESCALATE generates complete sets of instructions for the human operators (e.g., stock solution preparation) and the input files used by the robot to perform the experiments. ESCALATE is then used to capture the complete set of operator actions, ambient conditions, operator observations, and instrument log files associated with each reaction, along with relevant metadata.[64] Although the experiment generation and data management processes could have been performed manually, ESCALATE automated and accelerated these processes to meet the requirements for high-throughput experimentation. Among the observational data is a visual score of crystallite size for each reaction vial, following the scheme of our previous work and that of Cooper and co-workers.[60,67] Photographs of reaction vials are captured and reaction outcomes are scored into four classes: (1) clear solution without any solid; (2) fine powder; (3) small crystallites (average crystal dimension <0.1 mm); and (4) large (>0.1 mm) crystals suitable for structure determination by single crystal X-ray diffraction (see Crystal Scoring Rubric in the SI and examples of crystal images and their scores in Table S1 and Figure S2). The entire life-cycle of an experiment is shown in Figure S3. The complete data set from these reactions, including outcomes, crystal images, X-ray diffraction patterns, and modeling, is accessible via the SI; these data can be analyzed and visualized interactively using the online scripts provided[68] (see Interactive Data Visualization and Analysis Interface section in the SI). Detailed descriptions of the experimental and computed features used for this work are provided in the SI. Crystallization outcomes, and the features of the experiments that produced them, are tabulated in a comma-separated-value (CSV) file publicly available at https://github.com/darkreactions/rapid.[69]

High-Throughput Screening. A total of 8172 ITC reactions were performed in 45 different chemical systems, each of which contains lead(II) iodide and an organic cation. Here, 45 structurally diverse organoammoniums are chosen as organic cations, including aliphatic ammonium ions [e.g., methylammonium (MA), ethylammonium (EtA)]; aromatic cations [e.g., phenethylammonium (PhenEtA), benzylammonium (BenA)]; linear chains [e.g., *n*-butylammonium (nBuA), *n*-dodecylammonium (nDodA)]; branched structures [e.g., iso-butylammonium (iBuA), acetamidinium (Acet)]; cyclic cations [e.g., cyclohexylmethylammonium (CHMA)]; secon-

https://dx.doi.org/10.1021/acs.chemmater.0c01153
Chem. Mater. 2020, 32, 5650−5663

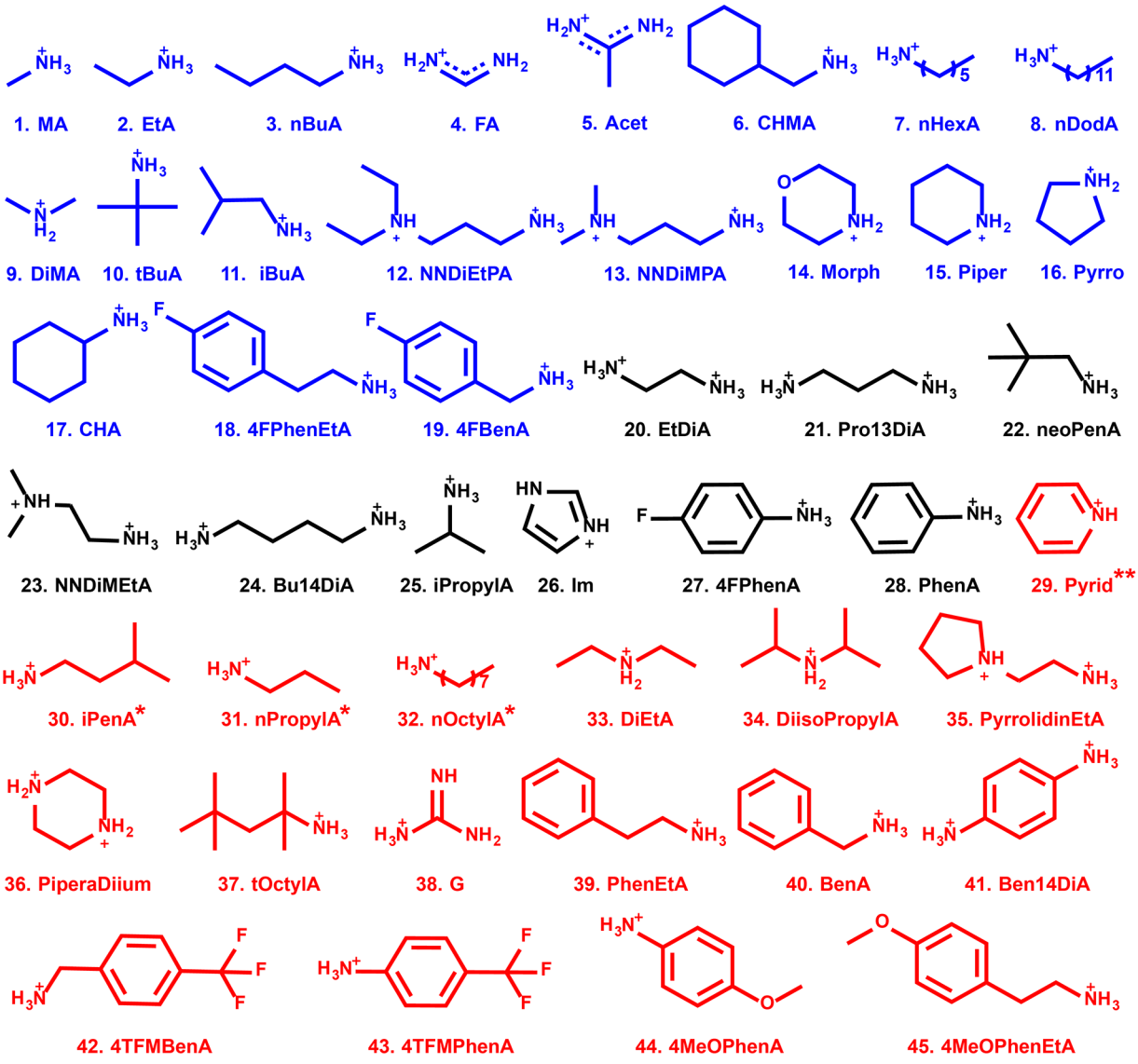

Figure 1. Chemical structures of the organoammonium cations studied in this work (see Table S2 for full chemical names). Blue-colored structures produce Class 4 large crystals confirmed to be perovskite-derived phases. Black structures produce Class 4 crystals with unknown structure (i.e., powder-XRD patterns do not match any known phases of perovskite-derived compounds, PbI_2, or organoammonium iodides). Red-colored cations produce only Class 1−3 outcomes or PbI_2 crystals. Single asterisk (*) indicates cations producing Class 3 outcomes with unknown phase. Double asterisk (**) indicates Class 3 outcomes confirmed as a perovskite-derived phase.

dary and tertiary ammoniums [e.g., *N*,*N*-diethylpropane-1,3-diammonium (NNDiEtPA)]; and amidinium ions [e.g., formamidinium (FA)]. Chemical structures and abbreviations for these 45 organoammoniums are shown in Figure 1. These compounds comprise all of the organoammonium iodides sold by the vendor (GreatCell Solar Materials.), providing a survey of the most accessible region of chemical space and the one most replicable by other chemists. Reactions within a given system vary in their lead iodide, organoammonium iodide and formic acid concentrations. As shown in Figures 2, S5, and S6, high-throughput screening allowed for the identification of conditions that result in large crystals (indicated by red circles) for each chemical system, demonstrating the efficacy of exploratory work using this automated workflow. Whereas only methylammonium (MA) and formamidinium (FA) halide perovskites were previously known to form via ITC,[34−36] we find that ITC is possible for perovskites that incorporate organoammonium cations with a much wider range of molecular weights, degree of ammonium substitution, and structural features such as aliphatic and aromatic rings. The high-throughput screening results for all 45 chemical systems are accessible through our interactive data visualization and analysis interface (For example images, see Figure S1).[68]

The conditions for which large, macroscopic crystals grow often cluster in a single region of chemical concentration space for each chemical system, with cluster positions varying between systems. For the synthesis of $EtAPbI_3$ at 95 °C (Figure 2b), large, Class 4 crystals are formed in the intermediate inorganic and organic concentration regime (0.3−0.8 M and 1−2 M, respectively) with a high concentration of formic acid (>6.0 M). Higher lead iodide concentrations tend to produce fine powders (Class 2) because such high PbI_2 concentrations induce faster nucleation. Conversely, lower concentrations of lead iodide do not result in any solid product.[15] The observation that adding formic acid facilitates crystallization is consistent with reports by Snaith

https://dx.doi.org/10.1021/acs.chemmater.0c01153
Chem. Mater. 2020, 32, 5650−5663

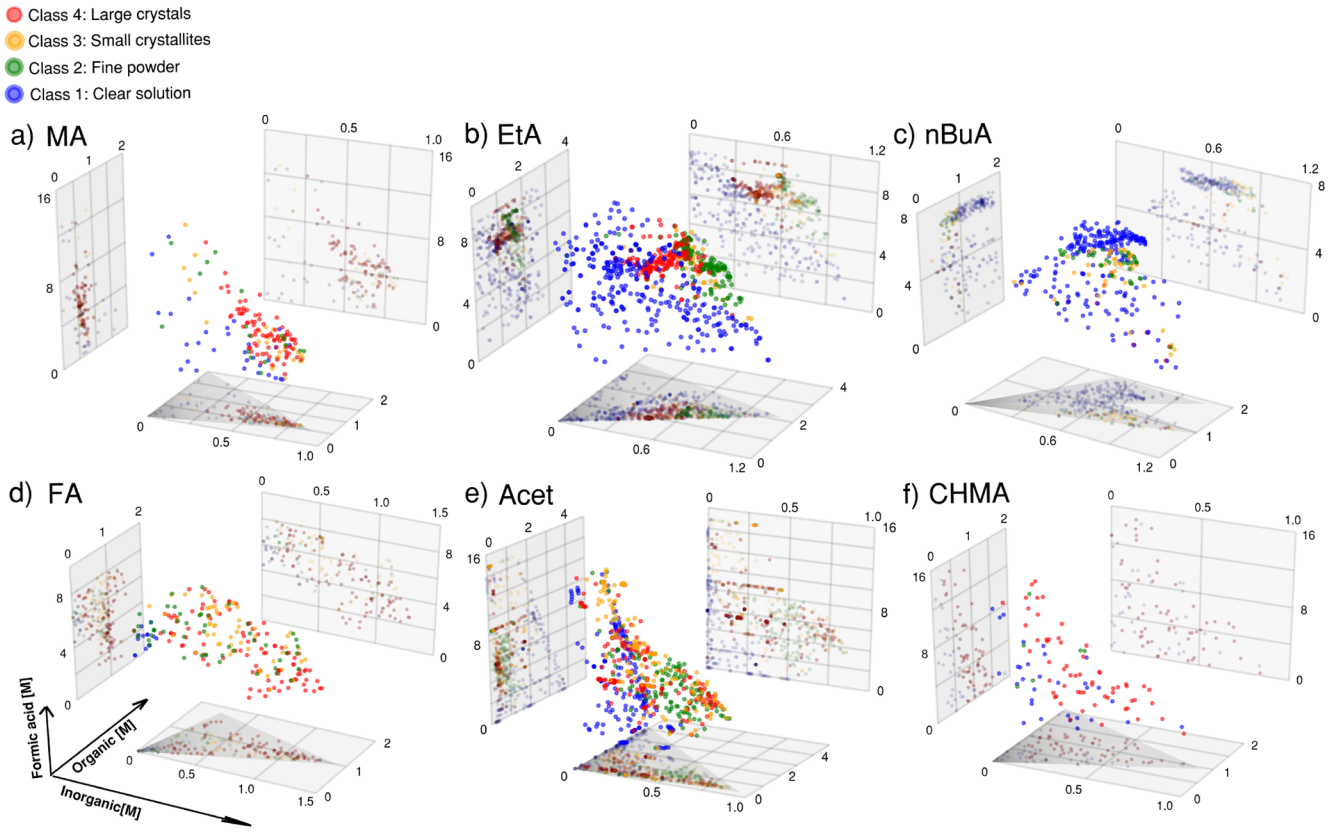

Figure 2. Crystal quality of 2295 lead iodide perovskite reactions as a function of the organic cation and the concentrations of the organic, inorganic (PbI_2), and formic acid precursors. Organic precursors are methylammonium iodide (a), ethylammonium iodide (b), *n*-butylammonium iodide (c), formamidinium iodide (d), acetamidinium iodide (e), and cyclohexylmethylammonium iodide (f). Reactions shown were performed at 95 °C. Light gray boxes show two-dimensional projections of the data. Dark gray triangles illustrate the accessible experimental space in the organic–inorganic plane, as constrained by precursor solubilities. Additional data for other organoammonium precursors are shown in Figures S5 and S6 and in the interactive data visualization interface.[68]

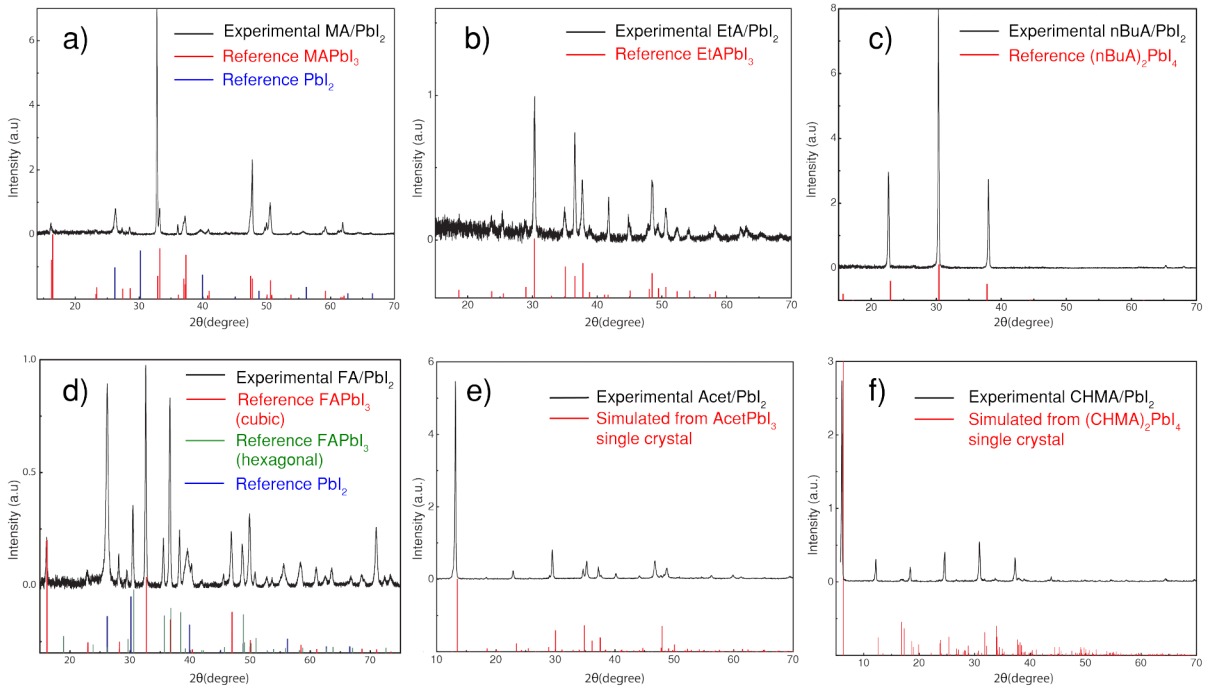

Figure 3. Powder X-ray diffraction patterns of crystals grown from the following systems: MA/PbI_2 (a), EtA/PbI_2 (b), $nBuA/PbI_2$ (c), FA/PbI_2 (d), $Acet/PbI_2$ (e), and $CHMA/PbI_2$ (f). See text for ICSD numbers for reference patterns.

https://dx.doi.org/10.1021/acs.chemmater.0c01153
Chem. Mater. 2020, 32, 5650−5663

and co-workers;[70] increasing the acidity of the reaction solution dissolves PbI_x colloid intermediates, raising the effective lead and iodide concentrations, and in turn promoting metal halide perovskite single crystal formation.

Powder X-ray diffraction measurements (pXRD) performed on ground, Class 4 samples from RAPID reactions indicate that tetragonal $MAPbI_3$[30,71] was successfully synthesized from the MA/PbI_2 reaction system (Figure 3a). The FA/PbI_2 system predominantly produced cubic $FAPbI_3$ mixed with the hexagonal phase (Figure 3d), which is not surprising in light of the bistability of this compound and its propensity toward phase transitions.[72,73] Some PbI_2 impurity (ICSD #52370) was also observed in the MA/PbI_2 and FA/PbI_2 systems due to the decomposition of the perovskite phases between synthesis and characterization.[74,75] Our ability to quickly explore possible reaction conditions to yield both $MAPbI_3$ and $FAPbI_3$ demonstrates the utility of RAPID for the formation of metal halide perovskites. Additional pXRD patterns indicate that orthorhombic $EtAPbI_3$[76,77] (Figure 3b), orthorhombic $(nBuA)_2PbI_4$[78,79] (Figure 3c), and 13 other metal halide perovskites (Figures S7−S19) were crystallized using ITC methods.

Powder XRD patterns from the Acet/PbI_2 system (Figure 3e) did not match simulated XRD patterns (Figure S20) for calculated structures of $AcetPbI_3$,[80] and no experimental structures have been reported for either Acet/PbI_2 or CHMA/PbI_2 (Figure 3f). This suggests that our high-throughput experiments revealed the presence of two previously unknown compounds, which we confirm below. To the best of our knowledge, ITC crystallization of the other 17 compounds shown in Figures 3 and S7−S19 (excluding $MAPbI_3$ and $FAPbI_3$) have not been previously reported, which demonstrates the utility of RAPID for discovering new synthetic routes. For the remaining 26 systems (i.e., those not shown in Figures 3 or S7−S19), nine of them produced large Class 4 crystals of unknown structures (i.e., unreported perovskite-derived phases, lead iodide or ammonium iodides, colored black in Figure 1) and another four cations produced Class 3 small crystals that are either perovskite-derived phases or unknown phases (marked with ** and * respectively in Figure 1). The remaining 13 chemical systems (colored red in Figure 1, without marks) only produced Class 1, Class 2, or lead iodide crystals. The pXRD patterns for all 45 chemical systems are available through the interactive data visualization interface.[68] These results suggest that additional screening, supplemented by high-throughput XRD, may be necessary for identifying perovskite-derived phases in those systems.

Crystal Structure Determination. The use of high-throughput experimentation in the RAPID approach described here enables the direct elucidation and optimization of crystal growth conditions. The optimized reaction conditions, determined using RAPID, were then validated with bench scale reactions for each system. The result was the formation of very large (>1 mm), high-quality single crystals (Figure 4) without the need for subsequent optimization. Crystals from the MA/PbI_2 and FA/PbI_2 systems were dodecahedral, consistent with prior literature reports for their ITC syntheses.[30,73] Crystals from the EtA/PbI_2 systems were irregularly shaped, while reactions in the nBuA/PbI_2 and CHMA/PbI_2 systems produced flake-like crystals similar to those reported for 2D perovskite structures.[78] Reactions in the Acet/PbI_2 system resulted in yellow needle-like crystals. All of these large crystals are suitable for single crystal X-ray diffraction studies. The ability to grow such large, high quality crystals after a single set of high-throughput experiments will accelerate materials discovery.

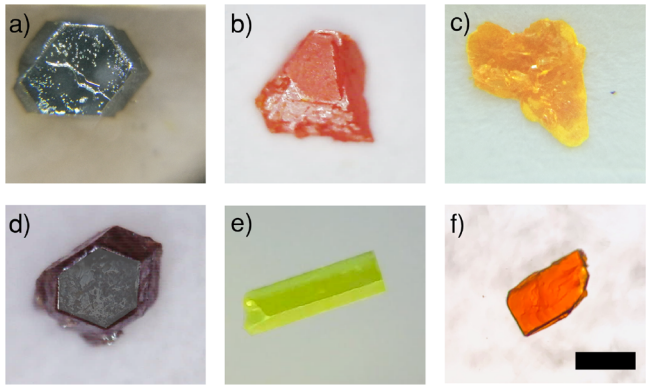

Figure 4. Optical micrographs of metal halide perovskite crystals produced by the MA/PbI_2 (a), EtA/PbI_2 (b), nBuA/PbI_2 (c), FA/PbI_2 (d), Acet/PbI_2 (e), and CHMA/PbI_2 systems (f). Scale bar: 1 mm.

The yellow crystals shown in Figure 4e and the orange crystals in Figure 4f are based upon the unidentified phases in the Acet/PbI_2 and the CHMA/PbI_2 systems, respectively. Structural determination based on single-crystal X-ray diffraction confirmed two new phases: $AcetPbI_3$ crystallizes in $P31m$ while $(CHMA)_2PbI_4$ crystallizes in $P2_1/c$. Crystallographic details are provided in Table 1, while tables of bond lengths and angles are listed in the SI.

Table 1. Crystallographic Data for $AcetPbI_3$ and $(CHMA)_2PbI_4$

compound	$AcetPbI_3$	$(CHMA)_2PbI_4$
formula	$C_2H_7I_3N_2Pb$	$C_{14}H_{32}I_4N_2Pb$
fw	646.98	943.24
space-group	$P31m$ (no. 157)	$P2_1/c$ (no. 14)
a (Å)	15.2648(6)	16.5155(8)
b (Å)	15.2648(6)	8.6521(5)
c (Å)	8.1332(3)	8.7642(4)
α (deg)	90	90
β (deg)	90	99.0461(19)
γ (deg)	120	90
V (Å^3)	1641.25(14)	1236.77(11)
Z	6	2
ρ_{calc} (g cm^{-3})	3.928	2.533
λ (Å)	0.71073	0.71073
T (K)	100(2)	100(2)
μ (mm^{-1})	23.820	11.811
R_1[a]	0.0365	0.0350
wR_2[b]	0.0658	0.0935

[a] $R_1 = ||F_o| - |F_c||/|F_o|$. [b] $wR_2 = [w(F_o^2 - F_c^2)^2/w(F_o^2)^2]^{1/2}$

The structure of $AcetPbI_3$, shown in Figure 5a, consists of one-dimensional $[PbI_{6/2}]^-$ chains separated by Acet cations. The $[PbI_{6/2}]^-$ chains are constructed from face shared octahedra. The asymmetric unit contains four distinct lead sites and four distinct iodine sites. This results in two unique $[PbI_{6/2}]^-$ chains, one of which contains Pb1, Pb2, I1 and I2, while the other contains Pb3, Pb4, I3, and I4. The Pb−I bonds range between 3.189(3) and 2.235(2) Å. The $[PbI_{6/2}]^-$ chains are aligned along the c-axis. An extensive hydrogen-bonding

https://dx.doi.org/10.1021/acs.chemmater.0c01153
Chem. Mater. 2020, 32, 5650−5663

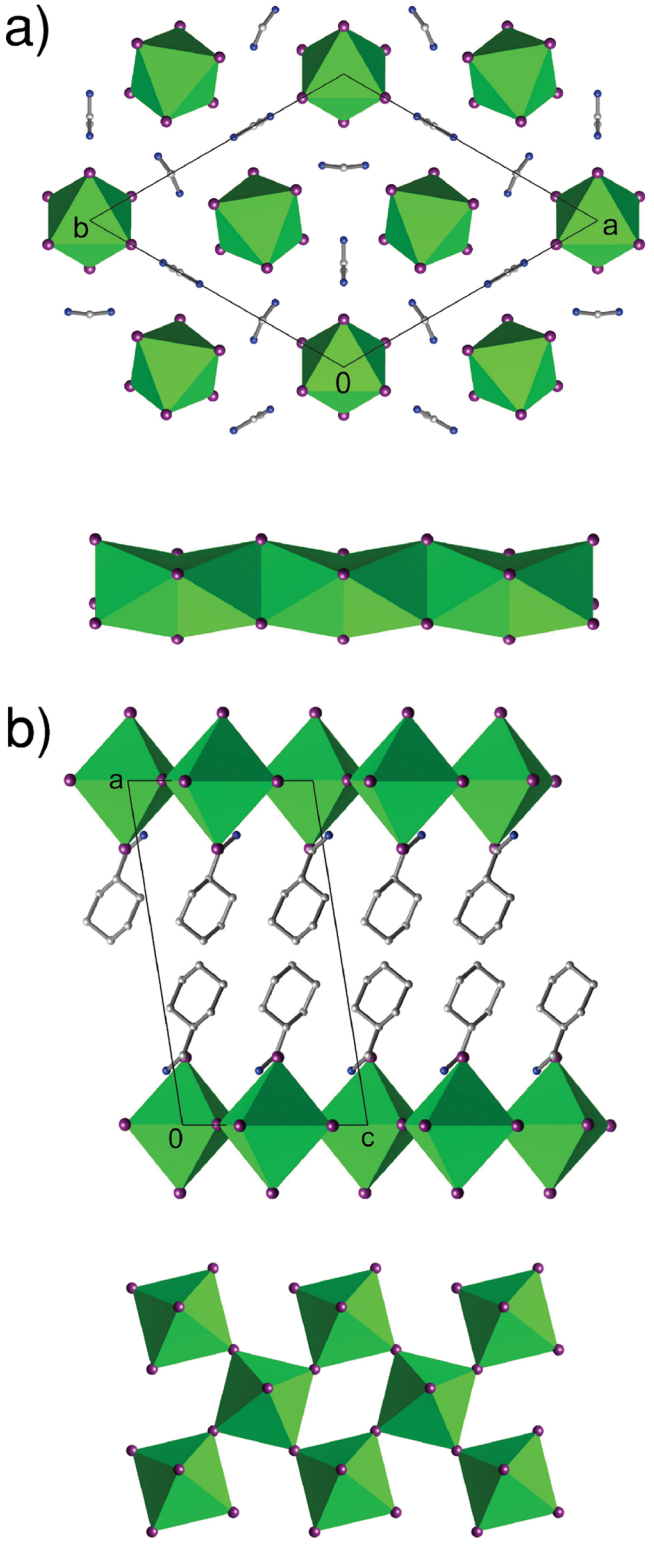

Figure 5. Three-dimensional packing and $[PbI_{6/2}]^-$ chain structure in $AcetPbI_3$ (a) and the three-dimensional packing and $[PbI_{2/1}I_{4/2}]^{2-}$ layer structure in $(CHMA)_2PbI_4$ (b). Green polyhedra represent $[PbI_6]$ octahedra, while purple, white, and blue atoms correspond to iodine, carbon, and nitrogen, respectively. Hydrogen atoms have been removed for clarity.

network exists between the Acet cations and $[PbI_{6/2}]^-$ chains. The structure of $AcetPbI_3$ is similar to the recently reported structure of pyrrolidinium lead iodide, which has a narrow optical bandgap and decent water resistance.[81]

The structure of $(CHMA)_2PbI_4$, shown in Figure 5b, contains two-dimensional $[PbI_{2/1}I_{4/2}]^{2-}$ layers and CHMA cations. The $[PbI_{2/1}I_{4/2}]^{2-}$ layers are constructed from corner shared octahedra. These layers are similar to those found in Ruddlesden−Popper phase perovskites.[78] The asymmetric unit contains a single lead site and two distinct iodine sites. The $Pb-I_{terminal}$ bonds have distances of 3.2129(5) Å, while the $Pb-I_{briding}$ distances range between 3.1680(4) and 3.1729(4) Å. The $[PbI_{2/1}I_{4/2}]^{2-}$ layers lie in the *ab* plane and are separated by the organic cations. An extensive hydrogen-bonding network exists between the CHMA cations and $[PbI_{2/1}I_{4/2}]^{2-}$ layers. The ammonium sites on the CHMA cations reside in the recesses within the $[PbI_{2/1}I_{4/2}]^{2-}$ layers. Details on the data collection, processing, and refinement of single crystal X-ray diffraction data for $AcetPbI_3$ and $(CHMA)_2PbI_4$ can be found in the SI.

As expected for 1D hybrid perovskite structures, whose electronic bands are less disperse than 3D perovskites,[82] the electrical conductivity of $AcetPbI_3$ single crystals is low, falling below the sensitivity limit of our measurement apparatus (2.8×10^{-11} S/cm, see SI: Conductivity Measurement and Figure S24). UV−visible absorption spectra and Tauc analyses suggest that $AcetPbI_3$ and $(CHMA)_2PbI_4$ have indirect bandgaps of 2.11 and 2.22 eV, respectively (Figures S21 and S22). While $(CHMA)_2PbI_4$ exhibits a green emission peak at 536 nm (40 nm full width at half-maximum, fwhm), $AcetPbI_3$ shows violet PL with an emission peak at 409 nm (54 nm fwhm) (Figure S23). The color-pure and short-wavelength PL makes $AcetPbI_3$ a potential candidate for violet and blue light-emitting diodes. Violet or blue PL is rarely reported for 1D-perovskite derivatives, which often show broader PL spectra at longer wavelengths due to the formation of self-trapped excitons.[81,83−85] Preliminary stability tests suggest that both $AcetPbI_3$ and $(CHMA)_2PbI_4$ are stable against humidity and oxygen over periods longer than 7 months; as shown in Figure S25, pXRD patterns of the two crystals exhibit no phase changes after storage in air at room temperature under 23−33% humidity. The identification and preliminary characterization of $AcetPbI_3$ and $(CHMA)_2PbI_4$ demonstrate the utility of RAPID to discover novel compounds with unexpected properties and environmental stability. More extensive investigations into the physical properties of the crystalline materials isolated in this work will be described elsewhere.

Quantifying Experimental Space and the Likelihood of Single Crystal Formation. The comprehensive sampling of the experimental space, facilitated by RAPID, enables the rigorous statistical analysis of reaction outcomes. To quantify the number of possible experiments for a given set of stock solutions, we calculated the volume V_{total} inside the convex hull (C_{total}) of the trials in the 19 crystallization screens which successfully result in the formation of large single crystals (Figures 2, S5, and S6). Here, C_{total} is the smallest convex polyhedral envelope containing all of the data points in multidimensional parameter space.[86] Differences in the reactant solubilities between organoammonium iodides result in convex hulls of different volumes. As shown in Figure 6b, the Piper/PbI_2 system exhibits the largest possible experimental space (as measured by C_{total}) followed by nHex/PbI_2, Morph/PbI_2, and Acet/PbI_2 in descending order. The nDodA/PbI_2 system exhibits the smallest V_{total} due to the poor

https://dx.doi.org/10.1021/acs.chemmater.0c01153
Chem. Mater. 2020, 32, 5650−5663

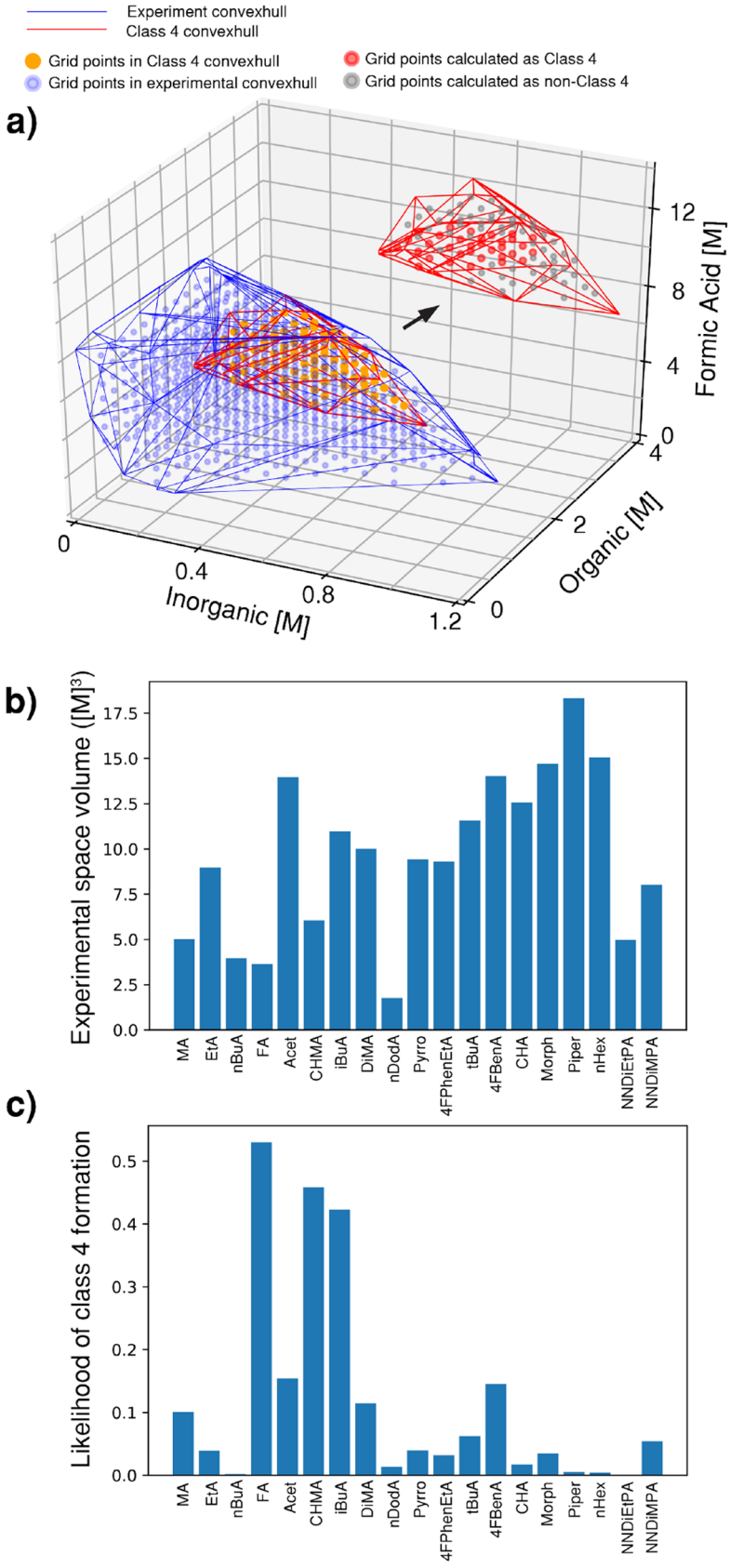

Figure 6. (a) Convex hulls, and the grid points contained within them, for the explored experimental space (blue lines/circles) and Class 4 outcomes (orange lines/circles), for the EtA/PbI_2 system at 95 °C. Inset: grid points within the Class 4 convex hull, with colors indicating Class 4 (red circles) and non-Class 4 (gray circles) outcomes as determined by the *k*-NN algorithm. (b) Convex hull volume of explored chemical space for all 19 perovskite syntheses. (c) Likelihood of large single crystal formation, P_4, for the 19 chemical systems studied.

https://dx.doi.org/10.1021/acs.chemmater.0c01153
Chem. Mater. 2020, 32, 5650−5663

solubility of *n*-dodecylammonium iodide and lead iodide/*n*-dodecylammonium iodide mixtures in GBL.

To quantify the volume of the regions in which single crystals can be grown for each system, the convex hulls containing all Class 4 outcomes were calculated (C_4, outlined in red in Figure 6a). C_4 includes some reactions that failed to generate single crystals (Classes 1−3, shaded in gray in Figure 6a), because the boundary between Class 4 and non-Class 4 is irregular. Therefore, the volume of C_4 will not accurately measure reaction success. Alternatively, the naïve approach of computing the ratio of number of successful reactions to the total number of observed reactions does not correctly describe the crystal formation probability because the distribution of reaction points is not homogeneous. A better estimate is obtained by interpolating the experimental data onto a uniform grid of points in the experimental space. C_{total} contains N_{total} of these grid points while C_4 contains N_4 points. Each grid point is assigned a crystal score using the 5 nearest experimental data points, following the *k*-nearest-neighbor (*k*-NN) algorithm with $k = 5$ (see SI for additional details on algorithm). This is a computationally tractable approximation to the generalized higher-order Voronoi tessellation.[87] The subset of $N_{(4)}$ grid points assigned to Class 4 scores using the *k*-NN method better accounts for the irregular (i.e., concave) envelopes. A graphical example is shown as an inset in Figure 6a for the EtA/PbI_2 system, with red circles denoting the $N_{(4)}$ points assigned to Class 4 with other crystal scores (N_4−$N_{(4)}$) indicated by gray circles. The corresponding plots for the other perovskite syntheses are shown in the SI (Figures S26−S43).

The likelihood of Class 4 formation (defined as $P_4 = N_{(4)}/N_{total}$) for the 19 systems in which metal halide perovskites were produced is shown in Figure 6c and Table S7. The FA/PbI_2, CHMA/PbI_2, and iBuA/PbI_2 systems show the highest likelihood of Class 4 crystal formation (P_4 = 0.53, 0.46, and 0.42 respectively) within the explored experimental space, followed by Acet/PbI_2 (0.15), 4FBenA/PbI_2 (0.15), DiMA/PbI_2 (0.11), and MA/PbI_2 (0.10). The other 12 systems show significantly lower P_4 values (<0.1) which indicate that for these systems, the formation of large perovskite crystals is thermodynamically less favorable over the vast majority of experimental space. In the perovskite literature, the Goldschmidt tolerance factor (calculated from the effective ionic radius of A-cation, B-cation and X-anion in the perovskite structure: ABX_3) is used to measure the stability and synthesizability of three-dimensional perovskite materials.[1,88] However, the 19 perovskite materials synthesized in this work are not necessarily three-dimensional. Thus, the P_4 value is not merely determined by the effective ionic radius but by a variety of factors. The formation of single crystals was rarely observed for $(nBuA)_2PbI_4$ and $(NNDiEtPA)_4Pb_5I_{18}$ syntheses, consistent with their low P_4 of 0.002 and 0.0001. The ability to quickly visualize the state space in each system and to quantify the crystal growth probabilities is a direct result of the high-throughput, parallelized experimental data collection enabled by the RAPID approach.

Machine Learning. Synthetic chemistry data sets often exclude failed results ("dark reactions")[60] and suffer from anthropogenic bias in experiment choices, limiting machine learning (ML) models trained on such data.[89] In contrast, RAPID's combination of high-throughput experimentation, randomized reaction parameters and complete data capture is ideal for training and evaluating machine learning models. As a demonstration, we exported ESCALATE's default set of 75 reaction conditions (e.g., concentrations, temperature, stir rate) and organic property descriptors (e.g., molecular weight, number of atoms, functional groups) and constructed a variety of machine learning models using the Scikit-Learn Python library (see SI and Methods for additional details). Binary classifier models were constructed to distinguish between experiments resulting in high quality single crystals (Class 4) and non-Class 4 outcomes. These models were applied to a base data set composed of the 4074 reactions in the 19 systems in which large crystals of metal halide perovskites were produced. Unless noted otherwise, each model was trained by randomly dividing the base data set into training and test sets (comprised of 80 and 20% of the data, respectively), with 5-fold cross-validation. The three models with the highest accuracy were as follows: Pearson VII Universal Function Kernel-based Support Vector Machine (PUFK-SVM), *k*-NN (where $k = 1$) and Radial Basis Function Kernel-based Support Vector Machine (RBFK-SVM) with respective accuracies of 0.869, 0.845, and 0.841 (complete results, including metrics such as recall and precision, are listed in Table S8). Our prediction quality on these 19 systems exceeds the 13% accuracy demonstrated for a comparable task on 3-picolylammonium lead bromide in previous work.[52] The good performance of the 1-NN approach is indicative of an interpolation (rather than extrapolation) problem,[90] which in turn is indicative of the high quality of the full, quasi-random-sampled data set. Learning curves for the six representative perovskites previously highlighted in Figures 2−4 using the accuracy, precision, recall, and F1 scores are shown in Figures S44−S49. The learning curves of the other 13 successful systems can be viewed in the interactive data visualization and analysis interface.[68] Training data and Python implementations of all of the models are available both in the interactive data visualization browser[68] and on the supporting GitHub repository.[69]

The ML models described above can be used to reduce the number of experiments needed to accurately predict successful crystallization conditions. As a test, the data were separated by A-cation identity, with the PUFK-SVM model performance being considered as a function of the number of training examples for each A-cation type. As expected, model predictions become more accurate with an increasing number of training experiments (Figure 7a); the model for the EtA/PbI_2 system achieves prediction accuracy as high as 85% with only ∼100 experiments. However, the flatness of the curves beyond 100 experiments indicates that a richer set of features (rather than more data) is needed to further improve the prediction quality. For $(nBuA)_2PbI_4$, the prediction accuracy decreases with an increasing number of training experiments, but this trend is an artifact of the low probability of Class 4 formation (P_4 = 0.002, Figure 6c). The early training rounds have no Class 4 outcomes, so the models are trained to predict only non-Class 4 outcomes, i.e., that all test samples will fail. The accuracy (formula given in the Software and Computation section in the SI) will be high even though the model fails to predict any of the positive outcomes. It is well-known that a heavily imbalanced distribution of class populations can result in accuracy values that do not capture the overall performance of the model, whereas the low precision and recall values for $(nBuA)_2PbI_4$ (Figure S46) do. As the number of training samples increases, and the model starts to predict successes, the accuracy when modeling the imbalanced test set is reduced.

https://dx.doi.org/10.1021/acs.chemmater.0c01153
Chem. Mater. 2020, 32, 5650−5663

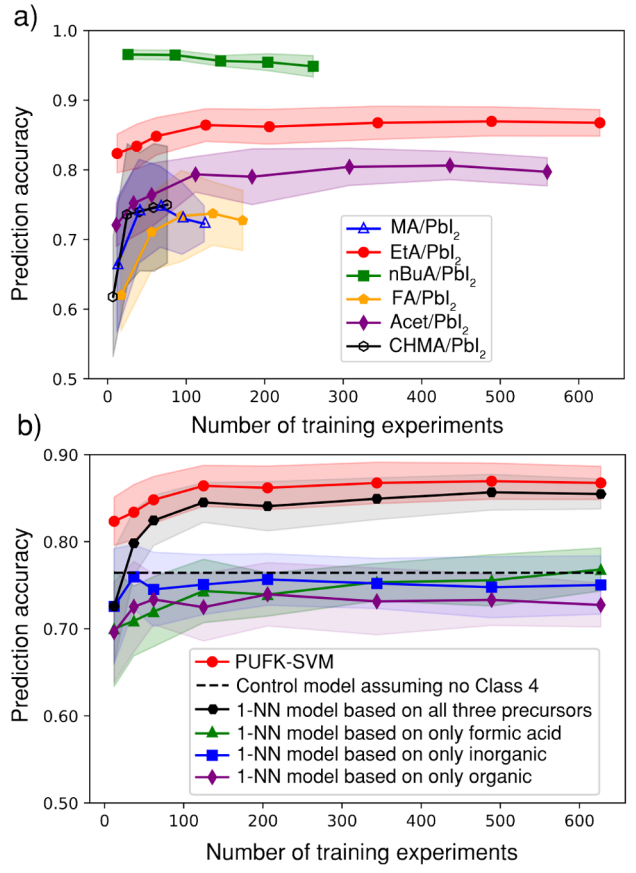

Figure 7. Learning curves for predicting perovskite crystal formation at 95 °C. (a) Prediction accuracy vs number of training experiments for PUFK-SVM models of the MA/PbI_2, EtA/PbI_2, $nBuA/PbI_2$, FA/PbI_2, $Acet/PbI_2$, and $CHMA/PbI_2$ system crystallization. Solid lines show mean accuracy distinguishing between Class 4 and non-Class 4 outcomes; shaded bands indicate the standard deviation from 5-fold cross validation results for each system. (b) Accuracy predicting EtA/PbI_2 Class 4 crystal formation for six different models: PUFK-SVM; a control model assuming no Class 4 crystals (dashed line); 1-NN models (k = 1) based on the concentrations of all three precursors (organic, inorganic, formic acid); and 1-NN models based on only one precursor.

As it might be useful to be able to predict fine powder and small crystallite growth conditions, we trained binary classification models for Class 1, Class 2, and Class 3 outcomes, individually, for the case of $EtAPbI_3$ (e.g., Class X = positive, non-Class X = negative, for X = 1, 2, 3). These results are shown in Figure S51. We found that our machine learning model (SVM with Pearson VII kernel) has the best performance predicting Class 1 (clear solutions) while having the lowest prediction metrics for Class 3. Predicting Class 2 outcomes is similar in performance to predicting Class 4 results. We hypothesize that the ML performance for different classes could be largely influenced by their distribution in experimental space (see Figure 2). Class 1 is easy to predict by the model as its reactions are distributed almost exclusively in a regularly shaped convex hull in the experimental space. The irregular distribution of Class 3 outcomes in the narrow space between Class 4 and Class 2 makes it the most difficult to predict.

ML models can assist in determining which experimental parameters contribute the most to the accuracy of the prediction, providing physical insight. As an illustrative example, we considered the EtA/PbI_2 system using only the concentrations of the organic, inorganic, and formic acid species. As depicted in Figure 7b, a PUFK-SVM model (red) trained exclusively on EtA/PbI_2 system data resulted in the highest performance, plateauing at 87% accuracy. For comparison, the control model (dashed line) that predicts every reaction to fail has 76% accuracy. Therefore, the PUFK-SVM predictions are significantly better than random chance. A 1-NN model (i.e., a k-NN with k = 1) in this three-dimensional feature space is 1−2% lower in absolute accuracy than the PUFK-SVM after 100 training experiments. This 1-NN algorithm is equivalent to using the most similar past reaction outcome as a prediction, and the high sample density of our data set facilitates this approach. Importantly, we find that the combination of the three reactant concentrations is meaningful. We demonstrated this by generating 1-NN models that only consider the concentration of a single reagent (green, blue, and purple lines in Figure 7b). These single variable models are less accurate than the control model, indicating that they have no predictive value. Taken together, these data support the reasonable conclusion that crystal quality is not determined by the concentration of a single chemical species, but instead depends on the concentrations of all species.

ML models can help generalize understanding across both reactions and reagent choices. As a demonstration, we used the PUFK-SVM model to predict reaction outcomes for each of the six representative perovskite systems studied given the following two training/testing strategies. The first strategy trained models using data only from the perovskite of interest. This baseline strategy corresponds to beginning the study of each organic cation with a tabula rasa. The second strategy trained ML models for a given cation of interest using data from the other N-1 organic cations as well. In principle, training data from other cations should improve prediction quality if the model can extract generalizable trends from the available chemical descriptors. However, the accuracies for both strategies (shown in Figure S50) are statistically indistinguishable for all cations tested, indicating that, despite the ability to generalize across reaction conditions (vide supra) for a single cation, the models do not generalize across different cations. This could arise from the limitations of the current chemical descriptors or from the type of reaction outcomes we choose to model. Our current research efforts are aimed at addressing this issue, e.g., by incorporating new molecular embeddings and reaction representations pertaining to crystal formation.

CONCLUSIONS

We have developed an automated, high-throughput robotic synthesis platform (Robot-Accelerated Perovskite Investigation and Discovery, or RAPID) for metal halide perovskite single crystal discovery. A total of 8172 reactions were performed using our RAPID workflow, spanning the large experimental space of inverse temperature crystallization in only ∼400 h of unattended operation. For comparison, the same number of reactions performed manually, at 10 reactions per day, would require over 800 days, or over 6000 h of human labor. We identified conditions that produce perovskite single crystals for 19 out of 45 target perovskite compositions, adding 17 new materials to the library of metal halide perovskites accessible via ITC (a 400% increase). Among these compounds are two novel perovskite species, $AcetPbI_3$ and $(CHMA)_2PbI_4$, for

https://dx.doi.org/10.1021/acs.chemmater.0c01153
Chem. Mater. 2020, 32, 5650−5663

which we reported the crystal structures and performed preliminary characterization. Our RAPID data set allowed us to quantify the probability of randomly finding a condition that produces single crystals. We also demonstrated the use of this data set to train machine learning models to improve common materials discovery tasks. Fewer than 100 experiments are typically required to build an informative model for a new organic cation species, but the current data set and features preclude generalization across organic cations. This initial study emphasizes the need to expand the chemical library and physicochemical descriptors[91] to further improve the ability of ML models to predict the crystallization conditions of new organic−inorganic metal halide perovskites. Nonetheless, RAPID is a powerful tool for accelerating perovskite discovery and can be readily extended to a broad range of synthetic routes and materials.[91,92]

EXPERIMENTAL SECTION

Materials. All reagents were purchased from commercial sources and used without further purification. Lead iodide, formic acid, dimethyl sulfoxide (DMSO), and dimethylformamide (DMF) were purchased from Sigma-Aldrich with 99%, ≥ 95%, ≥ 99.5%, and 99.8% purity, respectively. γ-Butyrolactone (GBL) (≥98%) was purchased from Spectrum Chemical. All 45 ammonium iodides used in this work were purchased from GreatCell Solar Materials with purity ≥98%.

Stock Solutions and Solubility Measurements. Before each robotic synthesis, stock solutions (ammonium iodide stocks and stocks containing mixtures of PbI_2/ammonium iodide) were prepared manually based on the solubility of these compounds. To determine the maximum solubility of lead iodide in a given solvent (GBL, DMSO, or DMF) and for a given ammonium iodide concentration, lead iodide was mixed with different amounts of a selected ammonium iodide and then the solvent was added gradually into the mixtures until the solids were completely dissolved. During the dissolution process, suspensions were stirred and heated in an oil bath at 450 rpm and 75 °C. The resulting solutions were allowed to cool to room temperature to confirm their stability. The solubilities of pure ammonium iodides were measured using the same procedure. Solubility data for lead iodide and individual ammonium iodides are shown in Table S2. All stock solutions were used within 8 h of their preparation.

Robotic Synthesis Workflow. High-throughput synthesis of metal halide perovskite single crystals was performed with a Hamilton Microlab NIMBUS4 liquid handling robot equipped with four independent micropipettors. Robotic protocols, programmed in Hamilton Method Editor software, imported experiment-specific reaction parameters, such as reagent volumes, reaction times, and shaking speeds, from Microsoft Excel .xls spreadsheets generated by the ESCALATE[64] software pipeline. In addition to specifying experimental parameters, ESCALATE was used to capture experimental results and observations following characterization of the products.

Reaction components (i.e., the stock solutions, pure solvent, and formic acid) were placed in designated locations on NIMBUS operation deck, as shown in Figure S4. Glass scintillation vials (8 × 43 mm^2 diameter × height), which served as reaction vessels, were loaded into a 96-well aluminum microplate (Symyx Technologies), which was placed on a Hamilton Heater Shaker II (HHS2) module on the NIMBUS deck. Robot protocols were then initiated, beginning with preheating the 96 empty vials in the HHS2 to 105 °C set temperature. After the HHS2 temperature reached 80 °C, the liquid handling robot dispensed into each reaction vial specified amounts of the pure solvent, PbI_2/ammonium iodide stock solution, ammonium iodide stock solution, and formic acid. The microplate was then vortexed at 750 rpm for 15 min, followed by dispensing of a second cycle of formic acid. After another 20 min of vortexing at 750 rpm, the resulting solutions were held at an actual solution temperature of 95 °C (105 °C set temperature) without shaking for 2.5 h to allow for crystal growth. During crystallization, the NIMBUS robot was left undisturbed, and air convection was minimized by closing the sash of the fume hood. Additional details are given in the "Robotic Workflow" section and Step-by-Step Robotic Procedure in the SI.

Crystal Scoring. To score reaction outcomes, reaction vials were inspected at different angles by eye. Reaction outcomes were scored into four classes. Class 1: no solid observed in the solutions. Class 2: fine powder observed with no visible crystal facets; under illumination, reflection is diffuse rather than specular. Class 3: small crystallites with approximate size 0.1 mm or smaller; distinct from Class 2 in exhibiting specular reflection at certain angles, indicating the presence of crystal facets. Class 4: large crystals (>0.1 mm) with straight edges and large area of specular reflection from crystal facets. When multiple crystal types were observed in the same vial, we used the highest score for each reaction.

Characterization. Powder X-ray diffraction measurements were performed on a Bruker AXS D8 Discover GADDS X-ray Diffractometer equipped with a Vantec-500 area detector operated at 35 kV/40 mA using Co Kα radiation (1.79 Å wavelength). Diffuse reflectance UV−visible absorption spectra of powders ground from large perovskite crystals were measured with an Agilent Cary-5000 UV−vis−NIR spectrophotometer. Photoluminescence spectra (PL) of powders ground from large perovskite crystals were measured using a Horiba Jobin Yvon Fluorolog-3 spectrofluorometer. PL spectra were collected from 365 to 650 nm with 1 nm wavelength steps and 0.01 s integration time per step. Conductivity measurements were performed on needle-shaped $AcetPbI_3$ single crystals (with lengths of 0.3−0.6 mm) using a customized probe station. The needle crystals were placed on double-sided tape on clean glass slides and carbon paste was applied at opposite ends of the needle crystals as electrodes. In this configuration, the cross-sectional area of electron transport is approximately the cross-sectional area of the needle crystals, which is in the range of 0.3−0.4 mm^2. Platinum probes were placed to form contacts with carbon electrodes, and a Keithley 2400 source meter was used to measure $I-V$ curves.

Software and Machine Learning. Scripts for data analysis and visualization were written in Python 3.6 in Jupyter notebooks using the following libraries: Numpy 1.14.6, Pandas 0.22.0, Scipy 1.0.1, Matplotlib 3.1.0 and Scikit-learn 0.19.2. We used the Quickhull algorithm implemented in Scipy to calculate convex hulls. For machine learning, a total of 75 features were selected to describe each perovskite single crystal synthesis reaction. Those features include eight reaction conditions and 67 computed property descriptors of organoammonium. Detailed explanations for the features used in this work are listed in Section 3 of the SI (Explanation of Features/Descriptors for Machine Learning Modeling). Experimental results were analyzed as a binary classification problem: Class 4 outcomes were considered as positive results while non-Class 4 outcomes were considered as negative results. A 5-fold cross-validation procedure was used to prepare training/testing data sets for machine learning modeling. For 5-fold cross-validation, there were 5 different train/test splits on the data set: in each split, 80% of the data was randomly drawn to train the machine learning model, while the remaining 20% of the data was reserved for testing. Model hyper-parameters were optimized using a grid search method with 5-fold cross-validation for highest prediction accuracy.

ASSOCIATED CONTENT

Supporting Information

The Supporting Information is available free of charge at https://pubs.acs.org/doi/10.1021/acs.chemmater.0c01153.

Detailed materials and methods; instructions for interactively visualizing and downloading data sets for all 45 chemical systems studied in this work; photographs of representative crystals; additional crystal quality plots and XRD patterns for 13 perovskite systems not shown in the main text; solubility data for all perovskite systems in this work; single crystal

https://dx.doi.org/10.1021/acs.chemmater.0c01153
Chem. Mater. 2020, 32, 5650−5663

structure refinement, absorption spectra, PL spectra, electrical conductivity, and stability tests for $AcetPbI_3$ and $(CHMA)_2PbI_4$; additional convex hull plots and data; additional tables and training curves summarizing prediction metrics for machine learning models; and features and descriptors used for training machine learning models (PDF)

Crystallographic data for $AcetPbI_3$ (CIF)

Crystallographic data for $(CHMA)_2PbI_4$ (CIF)

AUTHOR INFORMATION

Corresponding Authors

Joshua Schrier − *Department of Chemistry, Haverford College, Haverford, Pennsylvania 19041, United States; Department of Chemistry, Fordham University, The Bronx, New York 10458, United States;* orcid.org/0000-0002-2071-1657; Email: jschrier@fordham.edu

Alexander J. Norquist − *Department of Chemistry, Haverford College, Haverford, Pennsylvania 19041, United States;* Email: anorquis@haverford.edu

Emory M. Chan − *Molecular Foundry, Lawrence Berkeley National Laboratory, Berkeley, California 94720, United States;* orcid.org/0000-0002-5655-0146; Email: EMChan@lbl.gov

Authors

Zhi Li − *Molecular Foundry, Lawrence Berkeley National Laboratory, Berkeley, California 94720, United States*

Mansoor Ani Najeeb − *Department of Chemistry, Haverford College, Haverford, Pennsylvania 19041, United States*

Liana Alves − *Department of Chemistry, Haverford College, Haverford, Pennsylvania 19041, United States; Molecular Foundry, Lawrence Berkeley National Laboratory, Berkeley, California 94720, United States*

Alyssa Z. Sherman − *Department of Chemistry, Haverford College, Haverford, Pennsylvania 19041, United States*

Venkateswaran Shekar − *Department of Computer Science, Haverford College, Haverford, Pennsylvania 19041, United States*

Peter Cruz Parrilla − *Department of Chemistry, Haverford College, Haverford, Pennsylvania 19041, United States*

Ian M. Pendleton − *Department of Chemistry, Haverford College, Haverford, Pennsylvania 19041, United States*

Wesley Wang − *Molecular Foundry, Lawrence Berkeley National Laboratory, Berkeley, California 94720, United States; Department of Chemistry, University of California, Berkeley, Berkeley, California 94720, United States*

Philip W. Nega − *Molecular Foundry, Lawrence Berkeley National Laboratory, Berkeley, California 94720, United States*

Matthias Zeller − *Department of Chemistry, Purdue University, West Lafayette, Indiana 47907, United States;* orcid.org/0000-0002-3305-852X

Complete contact information is available at: https://pubs.acs.org/10.1021/acs.chemmater.0c01153

Notes

The authors declare no competing financial interest.

ACKNOWLEDGMENTS

This study is based upon work supported by the Defense Advanced Research Projects Agency (DARPA) under Contract No. HR001118C0036. Any opinions, findings, and conclusions or recommendations expressed in this material are those of the authors and do not necessarily reflect the views of DARPA. Work at the Molecular Foundry was supported by the Office of Science, Office of Basic Energy Sciences, of the U.S. Department of Energy under Contract No. DE-AC02-05CH11231. L.A. and J.S. were supported in part by the U.S. Department of Energy, Office of Science, Office of Workforce Development for Teachers and Scientists (WDTS) under the Visiting Faculty Program (VFP) and Berkeley Lab Undergraduate Faculty Fellowship (BLUFF). J.S. acknowledges the Henry Dreyfus Teacher-Scholar Award (TH-14-010). M.Z. acknowledges the National Science Foundation, Major Research Instrumentation Program under Grant No. CHE 1625543, for funding for the single crystal X-ray diffractometer.

REFERENCES

(1) Saparov, B.; Mitzi, D. B. Organic−Inorganic Perovskites: Structural Versatility for Functional Materials Design. *Chem. Rev.* **2016**, *116*, 4558−4596.

(2) Mitzi, D. B.; Feild, C. A.; Schlesinger, Z.; Laibowitz, R. B. Transport, Optical, and Magnetic Properties of the Conducting Halide Perovskite $CH_3NH_3SnI_3$. *J. Solid State Chem.* **1995**, *114*, 159−163.

(3) Herz, L. M. Charge-Carrier Mobilities in Metal Halide Perovskites: Fundamental Mechanisms and Limits. *ACS Energy Lett.* **2017**, *2*, 1539−1548.

(4) Xing, G.; Mathews, N.; Sun, S.; Lim, S. S.; Lam, Y. M.; Grätzel, M.; Mhaisalkar, S.; Sum, T. C. Long-Range Balanced Electron- and Hole-Transport Lengths in Organic-Inorganic $CH_3NH_3PbI_3$. *Science* **2013**, *342*, 344−347.

(5) Zhao, Y.; Zhu, K. Organic−Inorganic Hybrid Lead Halide Perovskites for Optoelectronic and Electronic Applications. *Chem. Soc. Rev.* **2016**, *45*, 655−689.

(6) Takahashi, Y.; Obara, R.; Nakagawa, K.; Nakano, M.; Tokita, J.; Inabe, T. Tunable Charge Transport in Soluble Organic−Inorganic Hybrid Semiconductors. *Chem. Mater.* **2007**, *19*, 6312−6316.

(7) Veldhuis, S. A.; Boix, P. P.; Yantara, N.; Li, M.; Sum, T. C.; Mathews, N.; Mhaisalkar, S. G. Perovskite Materials for Light-Emitting Diodes and Lasers. *Adv. Mater.* **2016**, *28*, 6804−6834.

(8) Wang, H.-C.; Bao, Z.; Tsai, H.-Y.; Tang, A.-C.; Liu, R.-S. Perovskite Quantum Dots and Their Application in Light-Emitting Diodes. *Small* **2018**, *14*, 1702433−1702455.

(9) Deschler, F.; Price, M.; Pathak, S.; Klintberg, L. E.; Jarausch, D.-D.; Higler, R.; Hüttner, S.; Leijtens, T.; Stranks, S. D.; Snaith, H. J.; et al. High Photoluminescence Efficiency and Optically Pumped Lasing in Solution-Processed Mixed Halide Perovskite Semiconductors. *J. Phys. Chem. Lett.* **2014**, *5*, 1421−1426.

(10) Hu, X.; Zhang, X.; Liang, L.; Bao, J.; Li, S.; Yang, W.; Xie, Y. High-Performance Flexible Broadband Photodetector Based on Organolead Halide Perovskite. *Adv. Funct. Mater.* **2014**, *24*, 7373−7380.

(11) Li, F.; Ma, C.; Wang, H.; Hu, W.; Yu, W.; Sheikh, A. D.; Wu, T. Ambipolar Solution-Processed Hybrid Perovskite Phototransistors. *Nat. Commun.* **2015**, *6*, 8238.

(12) Lee, W.; Li, H.; Wong, A. B.; Zhang, D.; Lai, M.; Yu, Y.; Kong, Q.; Lin, E.; Urban, J. J.; Grossman, J. C.; et al. Ultralow Thermal Conductivity in All-Inorganic Halide Perovskites. *Proc. Natl. Acad. Sci. U. S. A.* **2017**, *114*, 8693−8697.

(13) Pisoni, A.; Jaćimović, J.; Barišić, O. S.; Spina, M.; Gaál, R.; Forró, L.; Horváth, E. Ultra-Low Thermal Conductivity in Organic−Inorganic Hybrid Perovskite $CH_3NH_3PbI_3$. *J. Phys. Chem. Lett.* **2014**, *5*, 2488−2492.

(14) Correa-Baena, J.-P.; Abate, A.; Saliba, M.; Tress, W.; Jacobsson, T. J.; Grätzel, M.; Hagfeldt, A. The Rapid Evolution of Highly Efficient Perovskite Solar Cells. *Energy Environ. Sci.* **2017**, *10*, 710−727.

(15) Zhou, Y.; Game, O. S.; Pang, S.; Padture, N. P. Microstructures of Organometal Trihalide Perovskites for Solar Cells: Their Evolution from Solutions and Characterization. *J. Phys. Chem. Lett.* **2015**, *6*, 4827−4839.
(16) Correa-Baena, J.-P.; Saliba, M.; Buonassisi, T.; Grätzel, M.; Abate, A.; Tress, W.; Hagfeldt, A. Promises and Challenges of Perovskite Solar Cells. *Science* **2017**, *358*, 739−744.
(17) Giustino, F.; Snaith, H. J. Toward Lead-Free Perovskite Solar Cells. *ACS Energy Lett.* **2016**, *1*, 1233−1240.
(18) Huang, J.; Yuan, Y.; Shao, Y.; Yan, Y. Understanding the Physical Properties of Hybrid Perovskites for Photovoltaic Applications. *Nat. Rev. Mater.* **2017**, *2*, 17042.
(19) Wang, R.; Mujahid, M.; Duan, Y.; Wang, Z.-K.; Xue, J.; Yang, Y. A Review of Perovskites Solar Cell Stability. *Adv. Funct. Mater.* **2019**, *29*, 1808843−1808867.
(20) Best Research-Cell Efficiency Chart | Photovoltaic Research | NREL https://www.nrel.gov/pv/cell-efficiency.html (accessed Jun 24, 2019).
(21) Leveillee, J.; Katan, C.; Even, J.; Ghosh, D.; Nie, W.; Mohite, A. D.; Tretiak, S.; Schleife, A.; Neukirch, A. J. Tuning Electronic Structure in Layered Hybrid Perovskites with Organic Spacer Substitution. *Nano Lett.* **2019**, *19*, 8732−8740.
(22) Yang, C.; Peng, Y.; Simon, T.; Cui, T. Control of PbI_2 Nucleation and Crystallization: Towards Efficient Perovskite Solar Cells Based on Vapor-Assisted Solution Process. *Mater. Res. Express* **2018**, *5*, 045507−045516.
(23) Yin, J.; Qu, H.; Cao, J.; Tai, H.; Li, J.; Zheng, N. Vapor-Assisted Crystallization Control toward High Performance Perovskite Photovoltaics with over 18% Efficiency in the Ambient Atmosphere. *J. Mater. Chem. A* **2016**, *4*, 13203−13210.
(24) Deng, W.; Huang, L.; Xu, X.; Zhang, X.; Jin, X.; Lee, S.-T.; Jie, J. Ultrahigh-Responsivity Photodetectors from Perovskite Nanowire Arrays for Sequentially Tunable Spectral Measurement. *Nano Lett.* **2017**, *17*, 2482−2489.
(25) Shi, D.; Adinolfi, V.; Comin, R.; Yuan, M.; Alarousu, E.; Buin, A.; Chen, Y.; Hoogland, S.; Rothenberger, A.; Katsiev, K.; et al. Low Trap-State Density and Long Carrier Diffusion in Organolead Trihalide Perovskite Single Crystals. *Science* **2015**, *347*, 519−522.
(26) Dong, Q.; Fang, Y.; Shao, Y.; Mulligan, P.; Qiu, J.; Cao, L.; Huang, J. Electron-Hole Diffusion Lengths > 175 μm in Solution-Grown $CH_3NH_3PbI_3$ Single Crystals. *Science* **2015**, *347*, 967−970.
(27) Yue, H.-L.; Sung, H.-H.; Chen, F.-C. Seeded Space-Limited Crystallization of $CH_3NH_3PbI_3$ Single-Crystal Plates for Perovskite Solar Cells. *Adv. Electron. Mater.* **2018**, *4*, 1700655.
(28) Liao, W.-Q.; Zhang, Y.; Hu, C.-L.; Mao, J.-G.; Ye, H.-Y.; Li, P.-F.; Huang, S. D.; Xiong, R.-G. A Lead-Halide Perovskite Molecular Ferroelectric Semiconductor. *Nat. Commun.* **2015**, *6*, 7338−7344.
(29) Shi, C.; Ye, L.; Gong, Z.-X.; Ma, J.-J.; Wang, Q.-W.; Jiang, J.-Y.; Hua, M.-M.; Wang, C.-F.; Yu, H.; Zhang, Y.; et al. Two-Dimensional Organic−Inorganic Hybrid Rare-Earth Double Perovskite Ferroelectrics. *J. Am. Chem. Soc.* **2020**, *142*, 545−551.
(30) Saidaminov, M. I.; Abdelhady, A. L.; Murali, B.; Alarousu, E.; Burlakov, V. M.; Peng, W.; Dursun, I.; Wang, L.; He, Y.; Maculan, G.; et al. High-Quality Bulk Hybrid Perovskite Single Crystals within Minutes by Inverse Temperature Crystallization. *Nat. Commun.* **2015**, *6*, 7586−7592.
(31) Desai, S. Inverse Temperature Crystallization of Perovskite Material Methylammonium Lead Triiodide ($CH_3NH_3PBI_3$) and Its Applications for Energy Storage. Master's thesis, Lamar University: Beaumont, TX, 2017.
(32) Han, C.; Wei, Z.; Wang, K.; Yu, H.; Deng, L.; Zhu, X.; Yang, H.; Sun, X.; Zhao, F.; Zhang, Q.; et al. Effect of Surface Recombination in High Performance White-Light $CH_3NH_3PbI_3$ Single Crystal Photodetectors. *Opt. Express* **2018**, *26*, 26307−26316.
(33) Wang, K.-H.; Li, L.-C.; Shellaiah, M.; Sun, K. W. Structural and Photophysical Properties of Methylammonium Lead Tribromide ($MAPbBr_3$) Single Crystals. *Sci. Rep.* **2017**, *7*, 13643−13656.
(34) Kadro, J. M.; Nonomura, K.; Gachet, D.; Grätzel, M.; Hagfeldt, A. Facile Route to Freestanding $CH_3NH_3PbI_3$ Crystals Using Inverse Solubility. *Sci. Rep.* **2015**, *5*, 11654−11663.
(35) Najeeb, M. A.; Ahmad, Z.; Shakoor, R. A.; Alashraf, A.; Bhadra, J.; Al-Thani, N. J.; Al-Muhtaseb, S. A.; Mohamed, A. M. A. Growth of $MAPbBr_3$ Perovskite Crystals and Its Interfacial Properties with Al and Ag Contacts for Perovskite Solar Cells. *Opt. Mater.* **2017**, *73*, 50−55.
(36) Zhumekenov, A. A.; Saidaminov, M. I.; Haque, M. A.; Alarousu, E.; Sarmah, S. P.; Murali, B.; Dursun, I.; Miao, X.-H.; Abdelhady, A. L.; Wu, T.; et al. Formamidinium Lead Halide Perovskite Crystals with Unprecedented Long Carrier Dynamics and Diffusion Length. *ACS Energy Lett.* **2016**, *1*, 32−37.
(37) Chan, E. M.; Xu, C.; Mao, A. W.; Han, G.; Owen, J. S.; Cohen, B. E.; Milliron, D. J. Reproducible, High-Throughput Synthesis of Colloidal Nanocrystals for Optimization in Multidimensional Parameter Space. *Nano Lett.* **2010**, *10*, 1874−1885.
(38) Maryasin, B.; Marquetand, P.; Maulide, N. Machine Learning for Organic Synthesis: Are Robots Replacing Chemists? *Angew. Chem., Int. Ed.* **2018**, *57*, 6978−6980.
(39) Ahneman, D. T.; Estrada, J. G.; Lin, S.; Dreher, S. D.; Doyle, A. G. Predicting Reaction Performance in C−N Cross-Coupling Using Machine Learning. *Science* **2018**, *360*, 186−190.
(40) Lin, S.; Dikler, S.; Blincoe, W. D.; Ferguson, R. D.; Sheridan, R. P.; Peng, Z.; Conway, D. V.; Zawatzky, K.; Wang, H.; Cernak, T.; et al. Mapping the Dark Space of Chemical Reactions with Extended Nanomole Synthesis and MALDI-TOF MS. *Science* **2018**, *361*, eaar6236.
(41) Shevlin, M. Practical High-Throughput Experimentation for Chemists. *ACS Med. Chem. Lett.* **2017**, *8*, 601−607.
(42) Nikolaev, P.; Hooper, D.; Webber, F.; Rao, R.; Decker, K.; Krein, M.; Poleski, J.; Barto, R.; Maruyama, B. Autonomy in Materials Research: A Case Study in Carbon Nanotube Growth. *npj Comput. Mater.* **2016**, *2*, 16031.
(43) Duros, V.; Grizou, J.; Xuan, W.; Hosni, Z.; Long, D.-L.; Miras, H. N.; Cronin, L. Human versus Robots in the Discovery and Crystallization of Gigantic Polyoxometalates. *Angew. Chem., Int. Ed.* **2017**, *56*, 10815−10820.
(44) Ren, F.; Ward, L.; Williams, T.; Laws, K. J.; Wolverton, C.; Hattrick-Simpers, J.; Mehta, A. Accelerated Discovery of Metallic Glasses through Iteration of Machine Learning and High-Throughput Experiments. *Sci. Adv.* **2018**, *4*, eaaq1566.
(45) Reinhardt, E.; Salaheldin, A. M.; Distaso, M.; Segets, D.; Peukert, W. Rapid Characterization and Parameter Space Exploration of Perovskites Using an Automated Routine. *ACS Comb. Sci.* **2020**, *22*, 6−17.
(46) Lookman, T., Eidenbenz, S., Alexander, F., Barnes, C., Eds.; *Materials Discovery and Design: By Means of Data Science and Optimal Learning*; Springer International Publishing: Cham, Switzerland, 2018.
(47) Green, M. L.; Choi, C. L.; Hattrick-Simpers, J. R.; Joshi, A. M.; Takeuchi, I.; Barron, S. C.; Campo, E.; Chiang, T.; Empedocles, S.; Gregoire, J. M.; et al. Fulfilling the Promise of the Materials Genome Initiative with High-Throughput Experimental Methodologies. *Appl. Phys. Rev.* **2017**, *4*, 011105.
(48) Woo, S. I.; Kim, K. W.; Cho, H. Y.; Oh, K. S.; Jeon, M. K.; Tarte, N. H.; Kim, T. S.; Mahmood, A. Current Status of Combinatorial and High-Throughput Methods for Discovering New Materials and Catalysts. *QSAR Comb. Sci.* **2005**, *24*, 138−154.
(49) Koinuma, H.; Takeuchi, I. Combinatorial Solid-State Chemistry of Inorganic Materials. *Nat. Mater.* **2004**, *3*, 429−438.
(50) Chen, S.; Hou, Y.; Chen, H.; Tang, X.; Langner, S.; Li, N.; Stubhan, T.; Levchuk, I.; Gu, E.; Osvet, A.; et al. Exploring the Stability of Novel Wide Bandgap Perovskites by a Robot Based High Throughput Approach. *Adv. Energy Mater.* **2018**, *8*, 1701543.
(51) Xiang, X.-D.; Sun, X.; Briceño, G.; Lou, Y.; Wang, K.-A.; Chang, H.; Wallace-Freedman, W. G.; Chen, S.-W.; Schultz, P. G. A Combinatorial Approach to Materials Discovery. *Science* **1995**, *268*, 1738−1740.

https://dx.doi.org/10.1021/acs.chemmater.0c01153
Chem. Mater. 2020, 32, 5650−5663

(52) Kirman, J.; Johnston, A.; Kuntz, D. A.; Askerka, M.; Gao, Y.; Todorović, P.; Ma, D.; Privé, G. G.; Sargent, E. H. Machine-Learning-Accelerated Perovskite Crystallization. *Matter* **2020**, *2*, 938−947.
(53) Sun, S.; Hartono, N. T. P.; Ren, Z. D.; Oviedo, F.; Buscemi, A. M.; Layurova, M.; Chen, D. X.; Ogunfunmi, T.; Thapa, J.; Ramasamy, S.; Settens, C.; DeCost, B. L.; Kusne, A. G.; Liu, Z.; Tian, S. I. P.; Peters, I. M.; Correa-Baena, J.-P.; Buonassisi, T. Accelerated Development of Perovskite-Inspired Materials via High-Throughput Synthesis and Machine-Learning Diagnosis. *Joule* **2019**, *3*, 1437−1451.
(54) MacLeod, B. P.; Parlane, F. G. L.; Morrissey, T. D.; Häse, F.; Roch, L. M.; Dettelbach, K. E.; Moreira, R.; Yunker, L. P. E.; Rooney, M. B.; Deeth, J. R.; Lai, V.; Ng, G. J.; Situ, H.; Zhang, R. H.; Elliott, M. S.; Haley, T. H.; Dvorak, D. J.; Aspuru-Guzik, A.; Hein, J. E.; Berlinguette, C. P. Self-Driving Laboratory for Accelerated Discovery of Thin-Film Materials. *Science Advances* **2020**, *6*, eaaz8867.
(55) Li, J.; Lu, Y.; Xu, Y.; Liu, C.; Tu, Y.; Ye, S.; Liu, H.; Xie, Y.; Qian, H.; Zhu, X. AIR-Chem: Authentic Intelligent Robotics for Chemistry. *J. Phys. Chem. A* **2018**, *122*, 9142−9148.
(56) Lignos, I.; Morad, V.; Shynkarenko, Y.; Bernasconi, C.; Maceiczyk, R. M.; Protesescu, L.; Bertolotti, F.; Kumar, S.; Ochsenbein, S. T.; Masciocchi, N.; Guagliardi, A.; Shih, C.-J.; Bodnarchuk, M. I.; deMello, A. J.; Kovalenko, M. V. Exploration of Near-Infrared-Emissive Colloidal Multinary Lead Halide Perovskite Nanocrystals Using an Automated Microfluidic Platform. *ACS Nano* **2018**, *12*, 5504−5517.
(57) Lu, S.; Zhou, Q.; Ouyang, Y.; Guo, Y.; Li, Q.; Wang, J. Accelerated Discovery of Stable Lead-Free Hybrid Organic-Inorganic Perovskites via Machine Learning. *Nat. Commun.* **2018**, *9*, 3405.
(58) Tabor, D. P.; Roch, L. M.; Saikin, S. K.; Kreisbeck, C.; Sheberla, D.; Montoya, J. H.; Dwaraknath, S.; Aykol, M.; Ortiz, C.; Tribukait, H.; et al. Accelerating the Discovery of Materials for Clean Energy in the Era of Smart Automation. *Nat. Rev. Mater.* **2018**, *3*, 5.
(59) Balachandran, P. V.; Kowalski, B.; Sehirlioglu, A.; Lookman, T. Experimental Search for High-Temperature Ferroelectric Perovskites Guided by Two-Step Machine Learning. *Nat. Commun.* **2018**, *9*, 1668.
(60) Raccuglia, P.; Elbert, K. C.; Adler, P. D. F.; Falk, C.; Wenny, M. B.; Mollo, A.; Zeller, M.; Friedler, S. A.; Schrier, J.; Norquist, A. J. Machine-Learning-Assisted Materials Discovery Using Failed Experiments. *Nature* **2016**, *533*, 73−76.
(61) Correa-Baena, J.-P.; Hippalgaonkar, K.; van Duren, J.; Jaffer, S.; Chandrasekhar, V. R.; Stevanovic, V.; Wadia, C.; Guha, S.; Buonassisi, T. Accelerating Materials Development via Automation, Machine Learning, and High-Performance Computing. *Joule* **2018**, *2*, 1410−1420.
(62) Xu, R. J.; Olshansky, J. H.; Adler, P. D. F.; Huang, Y.; Smith, M. D.; Zeller, M.; Schrier, J.; Norquist, A. J. Understanding Structural Adaptability: A Reactant Informatics Approach to Experiment Design. *Mol. Syst. Des. Eng.* **2018**, *3*, 473−484.
(63) Braham, E. J.; Cho, J.; Forlano, K. M.; Watson, D. F.; Arròyave, R.; Banerjee, S. Machine Learning-Directed Navigation of Synthetic Design Space: A Statistical Learning Approach to Controlling the Synthesis of Perovskite Halide Nanoplatelets in the Quantum-Confined Regime. *Chem. Mater.* **2019**, *31*, 3281−3292.
(64) Pendleton, I. M.; Cattabriga, G.; Li, Z.; Najeeb, M. A.; Friedler, S. A.; Norquist, A. J.; Chan, E. M.; Schrier, J. Experiment Specification, Capture and Laboratory Automation Technology (ESCALATE): A Software Pipeline for Automated Chemical Experimentation and Data Management. *MRS Commun.* **2019**, *9*, 846−859.
(65) Brunetti, B.; Cavallo, C.; Ciccioli, A.; Gigli, G.; Latini, A. On the Thermal and Thermodynamic (In)Stability of Methylammonium Lead Halide Perovskites. *Sci. Rep.* **2016**, *6*, 31896.
(66) Fateev, S. A.; Petrov, A. A.; Khrustalev, V. N.; Dorovatovskii, P. V.; Zubavichus, Y. V.; Goodilin, E. A.; Tarasov, A. B. Solution Processing of Methylammonium Lead Iodide Perovskite from γ-Butyrolactone: Crystallization Mediated by Solvation Equilibrium. *Chem. Mater.* **2018**, *30*, 5237−5244.
(67) Wicker, J. G. P.; Cooper, R. I. Will It Crystallise? Predicting Crystallinity of Molecular Materials. *CrystEngComm* **2015**, *17*, 1927−1934.
(68) Shekar, V. et al. Interactive Data Visualization and Analysis Interface. https://mybinder.org/v2/gh/darkreactions/rapid/master?filepath=RAPID.ipynb (accessed Feb 25, 2020).
(69) Shekar, V. et al. RAPID Github Repository https://github.com/darkreactions/rapid (accessed Apr 23, 2020).
(70) Nayak, P. K.; Moore, D. T.; Wenger, B.; Nayak, S.; Haghighirad, A. A.; Fineberg, A.; Noel, N. K.; Reid, O. G.; Rumbles, G.; Kukura, P.; et al. Mechanism for Rapid Growth of Organic−Inorganic Halide Perovskite Crystals. *Nat. Commun.* **2016**, *7*, 13303.
(71) Stoumpos, C. C.; Malliakas, C. D.; Kanatzidis, M. G. Semiconducting Tin and Lead Iodide Perovskites with Organic Cations: Phase Transitions, High Mobilities, and Near-Infrared Photoluminescent Properties. *Inorg. Chem.* **2013**, *52*, 9019−9038.
(72) Weller, M. T.; Weber, O. J.; Frost, J. M.; Walsh, A. Cubic Perovskite Structure of Black Formamidinium Lead Iodide, α-$[HC(NH2)_2]PbI_3$, at 298 K. *J. Phys. Chem. Lett.* **2015**, *6*, 3209−3212.
(73) Saidaminov, M. I.; Abdelhady, A. L.; Maculan, G.; Bakr, O. M. Retrograde Solubility of Formamidinium and Methylammonium Lead Halide Perovskites Enabling Rapid Single Crystal Growth. *Chem. Commun.* **2015**, *51*, 17658−17661.
(74) Yang, J.; Siempelkamp, B. D.; Liu, D.; Kelly, T. L. Investigation of $CH_3NH_3PbI_3$ Degradation Rates and Mechanisms in Controlled Humidity Environments Using in Situ Techniques. *ACS Nano* **2015**, *9*, 1955−1963.
(75) Frost, J. M.; Butler, K. T.; Brivio, F.; Hendon, C. H.; van Schilfgaarde, M.; Walsh, A. Atomistic Origins of High-Performance in Hybrid Halide Perovskite Solar Cells. *Nano Lett.* **2014**, *14*, 2584−2590.
(76) Im, J.-H.; Chung, J.; Kim, S.-J.; Park, N.-G. Synthesis, Structure, and Photovoltaic Property of a Nanocrystalline 2H Perovskite-Type Novel Sensitizer $(CH_3CH_2NH_3)PbI_3$. *Nanoscale Res. Lett.* **2012**, *7*, 353.
(77) Safdari, M.; Fischer, A.; Xu, B.; Kloo, L.; Gardner, J. M. Structure and Function Relationships in Alkylammonium Lead(II) Iodide Solar Cells. *J. Mater. Chem. A* **2015**, *3*, 9201−9207.
(78) Stoumpos, C. C.; Cao, D. H.; Clark, D. J.; Young, J.; Rondinelli, J. M.; Jang, J. I.; Hupp, J. T.; Kanatzidis, M. G. Ruddlesden−Popper Hybrid Lead Iodide Perovskite 2D Homologous Semiconductors. *Chem. Mater.* **2016**, *28*, 2852−2867.
(79) Mitzi, D. B. Synthesis, Crystal Structure, and Optical and Thermal Properties of $(C_4H_9NH_3)_2MI_4$ (M = Ge, Sn, Pb). *Chem. Mater.* **1996**, *8*, 791−800.
(80) Kim, C.; Huan, T. D.; Krishnan, S.; Ramprasad, R. A Hybrid Organic-Inorganic Perovskite Dataset. *Sci. Data* **2017**, *4*, 170057.
(81) Xu, A. F.; Wang, R. T.; Britten, J. F.; Jarvis, V.; Yang, W.; Xu, G. Pyrrolidinium Lead Iodide from Crystallography: A New Perovskite with Low Bandgap and Good Water Resistance. *Chem. Commun.* **2019**, *55*, 3251−3253.
(82) Kaltzoglou, A.; Stoumpos, C. C.; Kontos, A. G.; Manolis, G. K.; Papadopoulos, K.; Papadokostaki, K. G.; Psycharis, V.; Tang, C. C.; Jung, Y.-K.; Walsh, A.; et al. Trimethylsulfonium Lead Triiodide: An Air-Stable Hybrid Halide Perovskite. *Inorg. Chem.* **2017**, *56*, 6302−6309.
(83) Yuan, Z.; Zhou, C.; Tian, Y.; Shu, Y.; Messier, J.; Wang, J. C.; van de Burgt, L. J.; Kountouriotis, K.; Xin, Y.; Holt, E.; et al. One-Dimensional Organic Lead Halide Perovskites with Efficient Bluish White-Light Emission. *Nat. Commun.* **2017**, *8*, 14051.
(84) Ma, C.; Shen, D.; Huang, B.; Li, X.; Chen, W.-C.; Lo, M.-F.; Wang, P.; Lam, M. H.-W.; Lu, Y.; Ma, B.; et al. High Performance Low-Dimensional Perovskite Solar Cells Based on a One Dimensional Lead Iodide Perovskite. *J. Mater. Chem. A* **2019**, *7*, 8811−8817.
(85) Seth, C.; Jana, D.; Jindal, V.; Khushalani, D.; Ghosh, S. One-Dimensional Behavior of Imidazolium Lead Iodide. *J. Phys. Chem. C* **2019**, *123*, 16449−16455.

https://dx.doi.org/10.1021/acs.chemmater.0c01153
Chem. Mater. 2020, 32, 5650−5663

(86) Berg, M.; de Cheong, O.; Kreveld, M.; van Overmars, M. *Computational Geometry: Algorithms and Applications*, 3rd ed.; Springer-Verlag: Berlin, 2008.
(87) Aurenhammer, F. Voronoi Diagrams—a Survey of a Fundamental Geometric Data Structure. *ACM Comput. Surv.* **1991**, *23*, 345−405.
(88) Travis, W.; Glover, E. N. K.; Bronstein, H.; Scanlon, D. O.; Palgrave, R. G. On the Application of the Tolerance Factor to Inorganic and Hybrid Halide Perovskites: A Revised System. *Chem. Sci.* **2016**, *7*, 4548−4556.
(89) Jia, X.; Lynch, A.; Huang, Y.; Danielson, M.; Lang'at, I.; Milder, A.; Ruby, A. E.; Wang, H.; Friedler, S. A.; Norquist, A. J.; Schrier, J. Anthropogenic Biases in Chemical Reaction Data and Their Detrimental Effect on Materials Discovery. *Nature* **2019**, *573*, 251−255.
(90) Wallach, I.; Heifets, A. Most Ligand-Based Classification Benchmarks Reward Memorization Rather than Generalization. *J. Chem. Inf. Model.* **2018**, *58*, 916−932.
(91) Pendleton, I. M.; Caucci, M. K.; Tynes, M.; Dharna, A.; Nellikkal, M. A. N.; Li, Z.; Chan, E. M.; Norquist, A. J.; Schrier, J. Can Machines "Learn" Halide Perovskite Crystal Formation Without Accurate Physicochemical Features? *J. Phys. Chem. C* **2020**, in press. DOI: 10.1021/acs.jpcc.0c01726.
(92) Yang, H.; Hamachi, L. S.; Rreza, I.; Wang, W.; Chan, E. M. Design Rules for One-Step Seeded Growth of Nanocrystals: Threading the Needle between Secondary Nucleation and Ripening. *Chem. Mater.* **2019**, *31*, 4173−4183.

https://dx.doi.org/10.1021/acs.chemmater.0c01153
Chem. Mater. 2020, 32, 5650−5663